HHS Public Access

Author manuscript

Phys Med Biol. Author manuscript; available in PMC 2024 July 10.

Published in final edited form as:

Phys Med Biol. ; 68(14): . doi:10.1088/1361-6560/ace09a.

Impact of a Novel Multilayer Imager on Metal Artifacts in MV-CBCT

TC Harris[1], **M Jacobson**[1], **M Myronakis**[1], **M Lehmann**[2], **P Huber**[2], **D Morf**[2], **I Ozoemelam**[1], **YH Hu**[1], **D Ferguson**[1], **R Fueglistaller**[2], **P Corral Arroyo**[2], **RI Berbeco**[1]

[1] Department of Radiation Oncology, Brigham and Women's Hospital, Dana Farber Cancer Institute and Harvard Medical School, Boston, MA, USA

[2] Varian Medical Systems, Baden-Dattwil, Switzerland

Abstract

Objective: Megavoltage cone-beam CT (MV-CBCT) imaging offers several advantages including reduced metal artifacts and accurate electron density mapping for adaptive or emergent situations. However, MV-CBCT imaging is limited by the poor efficiency of current detectors. Here we examine a new MV imager and compare CBCT reconstructions under clinically relevant scenarios.

Approach: A multilayer imager (MLI), consisting of four vertically stacked standard flat-panel imagers, was mounted to a clinical linear accelerator. A custom anthropomorphic pelvis phantom with replaceable femoral heads was imaged using MV-CBCT and kV-CBCT. Bone, aluminum, and titanium were used as femoral head inserts. 8MU 2.5MV scans were acquired for all four layers and (as reference) the top layer. Prostate and bladder were contoured on a reference CT and transferred to the other scans after rigid registration, from which the structural similarity index measure (SSIM) was calculated. Prostate and bladder were also contoured on CBCT scans without guidance, and Dice coefficients were compared to CT contours.

Main results: kV-CBCT demonstrated the highest SSIMs with bone inserts (prostate:0.86, bladder:0.94) and lowest with titanium inserts (0.32, 0.37). 4-layer MV-CBCT SSIMs were preserved with bone (0.75, 0.80) as compared to titanium (0.67, 0.74), outperforming kV-CBCT when metal is present. 1-layer MV-CBCT consistently underperformed 4-layer results across all phantom configurations. Unilateral titanium inserts and bilateral aluminum insert results fell between the bone and bilateral titanium results. Dice coefficients trended similarly, with 4-layer MV-CBCT reducing metal artifact impact relative to KV-CBCT to provide better soft-tissue identification.

Significance: MV-CBCT with a 4-layer MLI showed improvement over single-layer MV scans, approaching kV-CBCT quality for soft-tissue contrast. In the presence of artifact-producing metal implants, four-layer MV-CBCT scans outperformed kV-CBCT by eliminating artifacts and single-layer MV-CBCT by reducing noise. MV-CBCT with a novel multi-layer imager may be a valuable alternative to kV-CBCT, particularly in the presence of metal.

tharris@bwh.harvard.edu .

1. Introduction

Image guided radiation therapy (IGRT) is defined by imaging of patient anatomy immediately before, during, or after delivery of radiation delivery (Dawson 2007). IGRT is critical to state-of-the-art radiation therapy due to demonstrated increases in clinical control rates and reduced toxicity to healthy tissue (Bujold 2012). Tumors are not stationary, static targets, and can move or grow during or between treatments. IGRT enables more accurate and targeted therapy, permitting dose escalation and steeper dose gradients to protect nearby organs at risk. The imaging modality most commonly associated with IGRT is cone-beam CT (CBCT), an onboard technique that can provide three-dimensional data during a radiation therapy session (Jaffray 2002). CBCT uses a cone- rather than fan-based beam with one gantry revolution creating 3D volumetric data directly from acquired 2D projections. CBCT is an important component of IGRT, permitting more accurate treatment setup, online tumor and organ segmentation, and dose calculation.

Kilovoltage CBCT (kV-CBCT) and megavoltage CBCT (MV-CBCT) are two energy regimes employed for onboard imaging. Comparing the two modalities, kV-CBCT benefits from a much higher signal-to-noise ratio (SNR), driven largely by the higher detective quantum efficiency (DQE) of current flat panel imagers, compared to those used for MV-CBCT. kV is also more sensitive to differences in soft-tissue due to the physics of low-energy photons. Photoelectric effect interactions and their high Z dependence dominate at kV energies. The differential attenuation coefficients of the tissues imaged leads to better subject contrast. However, the sensitivity of kV imaging to atomic number can also result in large artifacts in the presence of metal (Barrett 2004). These streaking artifacts, caused by photon starvation, can obscure low contrast features in the reconstructed images. MV energy photons are more penetrating, and their interactions are primarily through Compton scattering. Thus, the scattering is not contingent on the material's atomic number but rather linearly dependent on electron density alone, leading to reduced subject contrast. However, MV photons are less affected by the presence of metal and other high Z materials. One way in which researchers are taking advantage of the reduced impact of atomic number on megavoltage imaging is by incorporating MV data with kV acquisitions to reduce metal artifacts while still retaining some of kV's greater subject contrast (Wu 2014, Jeon 2015).

MV-CBCT may also be used in treatment planning and/or dose calculation for adaptive radiotherapy or "see-and-treat" procedures. In adaptive radiotherapy with MV-CBCT, treatment plans are modified, and dose re-calculated, based on the current anatomy (Morin 2007, Thomas 2009). Segmentation of normal anatomy for adaptive radiotherapy is critical as those contours are the main basis on which adaptive decisions are made (Glide-Hurst 2021), thus any imaging study with adaptive applications should evaluate segmentation accuracy. In the case of adaptive prostate radiotherapy, bladder and rectum contours are often required for daily re-optimization and dose recalculation. For the latter, MV-CBCTs can be converted directly to electron density maps (Hughes 2012). In addition, MV-CBCT can have a role as the primary treatment planning imaging set for urgent radiation therapy, when there may not be the time or ability to acquire a planning CT (Held 2015).

Efforts to develop megavoltage beams for use in cone-beam CT have been pursued for some time (Mosleh-Shirazi 1998, Seppi 2003). Despite the progress made in designing efficient flat panel detectors, the use of MV imaging and potential benefits of MV-CBCT have been limited by the low DQE and low contrast of currently available electronic portal imaging devices (EPIDs) (Antonuk 2002). There has been considerable research directed at novel EPID construction to improve performance (Zhao 2004, Star-Lack 2015, Hu 2019). Monte Carlo simulation strategies have also been developed to aid in MV imager development (Shi 2020, Valencia Lozano 2021). The flat-panel imager used in the present study employs a multilayer architecture, vertically stacking four identical detection layers each analogous to current commercially available EPIDs. This multilayer imager (MLI) was found to increase performance metrics such as DQE and contrast-to-noise ratio (CNR) over single layer imagers (Harris 2020), while also conferring improvement to clinical EPID applications such as beam's-eye-view tumor tracking (Harris 2021). Furthermore, the MLI may provide better quality images at lower doses (Hu 2018, Myronakis 2020), and the layering can be used for spectral imaging (Myronakis 2018). In the current study, the quality of MV-CBCTs taken using a novel multilayer imager is compared against kV-CBCTs as well as MV-CBCTs taken using a single layer flat panel.

2. Materials and method

2.1 Multi-layer imager (MLI)

The 4-layer novel EPID employed in this study is differs from a version that was previously characterized by our group (Harris 2020). In addition to some electronics upgrades, the copper sheet were not included in the updated panel to improve CBCT performance. Each identical layer, vertically stacked, is comprised of a 0.436 mm (200 mg cm^{-2}) thick terbium-doped gadolinium oxysulfide (GOS) scintillator on top of a pixelated array of photodiode thin film transistors (hydrogen-doped amorphous silicon placed onto a glass substrate). Each layer operates like a Varian AS-1200 flat panel except for having a thicker scintillator (AS-1200's scintillator is 0.290 mm or 113 mg cm^{-2} thick).

The MLI's firmware enables operation in different modes, including collecting and averaging the response from all four layers or from the top layer only. These two modes enable a comparison between a 4-layer configuration versus a single-layer, similar to standard MV imaging. Prior work showed the four-layer MLI to have a DQE(0) of 9.7%, a 5.7 fold increase over what was measured for the standard single-layer Varian AS-1200 EPID (Harris 2020). In this previous study, CNR was found to nearly double (1.5x to 1.9x depending on the clinical application) when using four layers compared to one, with only a small decrease in resolution observed.

2.2 Phantom

A custom anthropomorphic pelvis phantom was commissioned (CIRS Inc, Norfolk, VA) which includes replaceable femoral head inserts (figure 1). The overall phantom dimensions are approximately 35 cm left-right, 20 cm ant-post, 26 cm sup-inf with anatomy from the L3 vertebra to mid-thigh. The femoral heads are modeled as 5 cm diameter spheres that come in three separate materials: trabecular bone equivalent, titanium, and aluminum; the latter

two materials represent possible metal implant materials. The phantom is designed so that the femoral heads can be replaced by removing the anterior half of the phantom, which does not disturb its positioning on the imaging couch. This feature allows serial scans to be taken with different inserts while not introducing any rotations or displacements.

2.3 Data acquisition

The phantom was placed in a standard GE CT scanner and imaged with the trabecular bone inserts for the femoral heads (120 kVp, 40 mAs, 0.25 cm slice thickness). This scan served as the ground truth for all subsequent imaging.

The CBCT experiments were carried out on a TrueBeam (Varian Medical Systems, Inc), which does not have native MV-CBCT capability. To address this, a developer mode script was written to read out the MV imager every 0.5 degrees for a full 360-degree arc. Each frame receives an average of 0.011 MU for a total of approximately 8 MU for the entire 720 frames. In order to avoid the horizontal banding that can occur due to asynchronous readout of the MV imager relative to beam pulses (Abbasian 2020), the script utilized the linac's gating circuit to initiate beam holds that allow proper syncing of the MV imager readout with beam pulses. The phantom was placed on the TrueBeam treatment couch, with isocenter aligned to the phantom prostate shape. Four different insert scenarios were considered: bilateral trabecular bone, bilateral titanium inserts, bilateral aluminum inserts, and unilateral titanium inserts. 2.5 MV CBCTs of the four scenarios were acquired using the developer mode script in two different sets: one with the MLI using all four of its layers, and one with the MLI using its top layer only, representing the response of a typical commercial EPID. 2.5 MV is a standard energy available on TrueBeam clinical linear accelerators. kV-CBCTs of these scenarios were acquired using a clinical pelvis preset (125 kVp and 1342 mAs).

Imaging dose was measured for the kV-CBCT and MV-CBCT techniques using the CTDI method (Shope 1981). A standard 32 cm diameter pelvis CTDI phantom was imaged with a 100 mm ionization chamber measuring output at 4 peripheral locations and a central cavity. The average of the peripheral readings contributed 2/3 of the CTDI value, and the central reading the remaining 1/3.

2-D spatial resolution has been previously reported by measured modulation transfer function (Harris 2020). Here, volumetric spatial resolution is assessed by conebeam imaging of a CatPhan phantom. Scans of the phantom were taken using the same kV, 4-layer MV, and 1-layer MV techniques described above for the pelvis phantom images. That is, the kV-CBCT was taken using a clinical preset at 125 kVp 1342 mAs and the MV-CBCTs used the developer mode script that enable 2.5 MV 8 MU acquisition.

2.4 Data processing

The MV-CBCT scans were reconstructed in iTools, a proprietary Varian reconstruction program which is based on their clinical reconstruction chain. All acquired projection views underwent flood-field and dark-field normalization, as well as scatter-removal and water-equivalent beam-hardening pre-corrections. Scatter correction used the fASKS kernel-based algorithm (Sun 2010) while the beam hardening correction used the now standard approach

of Joseph and Spital (Joseph 1978). Reconstruction of the pre-processed data used the FDK algorithm (Feldkamp 1984). Slick thickness was 0.2 cm. The kV-CBCT scans were reconstructed using the standard clinical TrueBeam CBCT reconstructor with the pelvis preset, which yields a 0.25 cm slice thickness.

2.5 Analysis

On the helical CT scan, the bladder and prostate were contoured by an ABR-certified clinical physicist. The bladder was present on 16 slices and had a volume of 49.2 cc. The prostate was also contoured on 16 slices and had a volume of 22.5 cc. This scan was rigidly registered to all of the CBCT scans, and the two contours were copied over. In addition, the bladder and prostate were drawn *de novo* on the CBCTs, without any assistance from the CT scan structures. All contouring was checked by two other ABR certified physicists.

All of the reconstructions and structure sets were imported into Matlab for analysis. Two metrics were calculated: the structure similarity index measure (SSIM) and the Dice similarity coefficient (DSC).

The SSIM is defined as (Wang 2004):

$$SSIM(x, y) = \frac{(2\mu_x\mu_y + c_1)(2\sigma_{xy} + c_2)}{(\mu_x^2 + \mu_y^2 + c_1)(\sigma_x^2 + \sigma_y^2 + c_2)}$$

Where for two similarly sized ROIs (x and y), μ is the average intensity, σ is the variance, and σ_{xy} is the covariance. The two c terms stabilize division when there is a weak denominator. In order to properly calculate the SSIM, a polynomial curve was used to fit the HU data of each scan setting air equal to 0 and a volume of muscle common to all scans equal to 1040, considering the HU for air and muscle are nominally −1000 and 40, respectively. The CT ground truth bladder and prostate structures were copied over to the registered CBCTs, and then had the SSIM calculated comparing those two regions in the CT and the CBCTs.

In order to investigate further the effect of metal artifacts on the various scans, three additional regions were drawn on the helical CT, and the standard deviation of their HU value assessed after the data fitting described in the previous paragraph. One ROI was a 1 cm diameter cylinder running the superior-inferior length of a femoral head. The cylinder is 2.6 cc and stays 5 mm from the bone edge and avoids the air gap created by the two halves of the phantom meeting (figure 2a). This ROI is expected to be significantly affected when metal inserts are present. Two other contours were drawn starting 1 cm superior to the femoral heads, where interference from metal inserts should be limited. One ROI is a 2 cm diameter cylinder near midline and in phantom material simulating fat tissue with a volume of 5.5 cc, the other cylinder has a diameter of 1 cm and volume of 2.6 cc, and is located in a muscle-simulating region near the left iliac crest (figure 2b). These three contours were transferred to the CBCTs using rigid registration. Additional contours were created by shifting these drawn structures 1.0 cm anterior, posterior, right, and left to increase the sampling points while containing the additional contours in their original muscle or fat material.

To mimic a potential clinical application of adaptive planning for CBCT, the prostate and bladder were contoured on all cone-beam reconstructions without referencing the ground truth contours drawn on the ground-truth CT. The newly created CBCT contours were compared with the CT contours after rigid registration via calculating their Dice similarity coefficient (DSC) by the standard equation (Dice 1945):

$$DSC(x, y) = \frac{2\,|x \cap y|}{|x| + |y|}$$

Where x and y are the contours segmented on the CT and the CBCT, respectively.

To analyze spatial resolution, we sampled voxel values in the vicinity of the curved surface edge of the Catphan604 phantom's Teflon insert. The samples were gathered over a full 360 degrees around the circumference of the insert and over a 1 cm axial section length. We then fit a 4-parameter Gaussian edge spread function (ESF) to these samples using the model equation shown in figure 3 where the unknown parameters are a,b,c, and d. Differentiating the fitted ESF in turn gave an estimate of the point spread function (PSF). The full-width at half maximum (FWHM) of the point spread function is equal to 2.355*c and was used to quantify and report the spatial blur in the image. Uncertainty in the calculated FWHMs were evaluated by repeating the calculation on subsets of the sampled voxel values.

Each subset was derived by partitioning the profile of the oversampled ESF (illustrated in figure 3) into 0.5 mm intervals and discarding random selections of half the samples in each of these intervals. One hundred random data subsets were generated in this manner and used to assess variability in the fitted FWHMs for each reconstructed CBCT image.

3. Results

A standard helical CT scan was taken of the phantom with bilateral trabecular inserts to serve as the ground truth (Figure 4). A helical scan yields the best image quality of the imaging modalities used in this study, and the trabecular inserts will cause the least amount of artifact, facilitating the most accurate delineation of regions of interest. Representative HU values from the reference CT scan were found to be −64 (fat), 67 (muscle), and 286 (bone), verifying that the phantom materials yield clinically observed electron densities. The imaging dose measured on a CTDI pelvis phantom was 23 mGy for the kV-CBCT and 33 mGy for the MV-CBCT.

Analysis of the spatial resolution using the Teflon insert boundary of the CatPhan yielded a kV PSF of 1.3 mm. The 4-layer MV PSF was 2.7 mm and 1-layer MV was 2.6 mm. A box and whisker plot is provided in figure 5.

A total of 8 MV-CBCT scans were acquired and reconstructed. Scans included 4-layer imaging of the phantom with bilateral trabecular bone inserts, bilateral aluminum inserts, bilateral titanium inserts, and unilateral titanium paired with unilateral trabecular inserts; this set was repeated with the MLI operating in 1-layer mode. 4 kV-CBCT scans were acquired and reconstructed, with one scan taken of each of the four phantom configurations. (Figure 6). Qualitatively, the metal inserts create considerable artifact in the kV scans – streaking

and photon starvation effects in particular – while the MV scans appear more robust to addition of higher Z inserts.

The structure similarity index measure (SSIM) was calculated for each acquisition scenario, as specified in Section 2.5. The results for the prostate and bladder calculations are plotted in Figure 7. The highest SSIMs were found in the kV scans with the bone inserts (prostate: 0.86, bladder: 0.94). The lowest SSIM occurred in kV scans with bilateral titanium implants inserted into the phantom (prostate: 0.32, bladder: 0.37). MV scans had SSIM ranges of 0.80 to 0.67 in 4-layer mode, and ranges of 0.73 to 0.63 in 1-layer mode. Aluminum and unilateral titanium SSIMs fell between the extremes of bilateral bone and bilateral titanium, with 4-layer MV-CBCT providing the best SSIMs. Overall, kV imaging of soft-tissue structures is substantially more impacted by the presence of any metal in the phantom.

The image HU standard deviation was evaluated in several ROIs as another measurement of image quality. Cylindrical ROIs were contoured on the helical CT scan as described in Section 2.5 and copied to the CBCT scans after rigid registration. The cylinders were translated within the same tissue type to give multiple sampling data points. The standard deviation in the ROI adjacent to the right femoral head and the average standard deviation of the ROIs distant from the femoral heads were evaluated, with the results shown in Figure 8. The standard deviation for the distant ROIs were consistent regardless of which material inserts were used, with average values of 15.5 for kV-CBCT, 17.5 for 4-layer MV-CBCT, and 28.5 for 1-layer MV-CBCT. However, the ROI adjacent to the femoral head shows a different trend, with 4-layer MV-CBCT having the lowest HU variability for all inserts and kV-CBCT the highest with metal inserts. The largest variation occurs in the double titanium insert scenario, with results of 154.7 +/− 32.6 for kV, 80.4 +/− 4.6 for 4-layer MV, and 88.8 +/− 6.7 for 1-layer MV. Overall, kilovoltage imaging sustained increased HU variability compared to 4-layer MV-imaging, especially when metal is near a ROI.

The Dice similarity coefficient (DSC) of de novo prostate and bladder contours on the CBCT scans were calculated by comparing with the ground truth from the kV-CBCT scans. The DSC calculation results for the prostate and bladder results are displayed in Figure 9. The maximum DSC was found in the kV scans with bone inserts (prostate: 0.97, bladder: 0.95), and the minimum determined to be in kV scans with bilateral titanium implants (prostate: 0.82, bladder 0.73). 4-layer MV DSC values ranged from 0.91 to 0.82 and 1-layer DSC values ranged from 0.87 to 0.75. Aluminum and unilateral titanium SSIMs fell between the extremes of bilateral bone and bilateral titanium, with 4-layer MV-CBCT providing the best SSIMs. ROIs contoured on an MV-CBCT taken with metal artifacts have better fidelity to the ground truth than ROIs segmented on kV-CBCT.

4. Discussion

In every scenario test, MV-CBCT with the 4-layer MLI demonstrated improved performance over the single layer MV imager. In the presence of metal artifacts, both 4-layer and single layer imagers are effective for reducing artifacts. This is because the beam hardening and photon starvation interactions between the beam and the phantom is not a function of imager architecture. In addition, MV-CBCT with the 4-layer MLI had improved evaluation metrics

relative to kV-CBCT for situations in the phantom having at least one metal insert. The difference was especially pronounced with two titanium inserts in the phantom, indicating that MV-CBCT will be most advantageous for situations where kV-CBCT will be most compromised by metal artifacts. kV-CBCT had superior metrics in the setting of trabecular bone inserts only, but the four-layer MLI's performance notably approached that of the kV imaging for this scenario. For example, the prostate SSIM with bone only: kV – 0.86, 4-layer MV – 0.75, 1-layer MV – 0.68.

The standard deviation of the HU for ROIs near and distant from the femoral heads are used as measures of noise and susceptibility to artifacts in the four different phantom configurations. The results for the ROIs distant from the femoral heads are consistent across the different scenarios, which tracks qualitatively with the lack of imaging artifact observed superior and inferior to the femoral heads. kV has the least deviation, with the 4-layer MV imaging showing performance approaching kV capabilities. The ratio of 4-layer:1-layer resultsis 0.6, which aligns with the theoretically expected impact of quadrupling the number of collected photons leading to a 0.5 reduction in noise. The results for the ROI in the immediate vicinity of the femoral heads reflect the influence of higher density materials. For this region, the 4-layer MV-CBCT yielded the least HU variability, even with only trabecular bone inserts present. kV results became considerable as the metal artifacts increased and was worst for the bilateral titanium inserts. The large error bars in the kV results suggest that imaging system noise is not solely responsible, and that metal artifacts are driving the increased variability. The 4-layer:1-layer ratio for the three scenarios with metal inserts was only 0.92, suggesting that photon starvation artifacts may limit some of the improvement offered by using multiple detecting layers.

Dice Similarity Coefficient of regions of interest (ROIs) contoured directly on the CBCTs compared to the CT ROIs offers insight into the clinical impact of the different imaging modalities. The MLI operating in 4-layer mode accomplished a higher DSC than kV-CBCT when metal was present, but kV-CBCT had the overall largest DSC with bone-only insert. The highest calculated DSC was 0.97 for the prostate contour on the bone-only kV-CBCT and the lowest observed DSC was 0.73 for the bladder contour on the bilateral titanium kV-CBCT. A possible explanation for the reduced DSC spread for de novo contours is that users with sufficient clinical experience may be able to accurately fill in the artifact regions of the ROI mentally. However, even in a setting where experienced oncologists and physicists are readily available, there may be value in contouring on MV-CBCT when metal implants are present, as it has been shown that segmenting ROIs on kV with hip prostheses leads to greater interobserver variability resulting in a lower conformity index and a higher coefficient of variation (Falcinelli 2015). Furthermore, segmenting an irregular and difficult to predict object such as a gross tumor volume may not benefit from the mental interpolation used when segmenting an organ, highlighting the importance of reduced artifact imaging.

For spatial resolution, the kV acquisition had the lowest PSF at 1.3 mm, with 4- and 1-layer MV scans having 2.7 mm and 2.6 mm PSFs, respectively. The 4- and 1-layer are similar and would not present a clinical difference in interpreting images. The separation between kV and MV PSF corresponds to about 2–3 voxels.

Prior studies comparing onboard imaging modalities typically focus on image quality metrics (Held 2016) that may not be applicable when substantial metal artifacts interfere. Methods to quantify metal artifacts vary; approaches based on measurements such as standard deviation within ROIs are common (Wellenberg 2017). ROI analysis was performed in this study, with SSIM additionally added to provide an objective metric of similarity between objects. DSC measurements provide a clinical metric in the context of a common onboard imaging scenario: contouring on treatment-day images. The bone-only kV results (SSIM: prostate – 0.86, bladder – 0.94; DSC: prostate – 0.97, bladder – 0.95) compare to other published with results, with SSIMs around 0.9 (Park 2017) and DSC (using a rigid phantom) around 0.9 (Landry 2017). Published results with metal implants are sparse and difficult to directly compare to this study. In a clinical setting, having better performance when evaluating ROIs, SSIM, and DSC means better ability to discern and segment structures on images taken immediately prior to treatment.

Imaging dose is an important consideration when evaluating clinical imaging modalities. Volumetric kV imaging has the CT dose index (CTDI), which allows easy dose comparison between modalities. However, no such method exists for MV-CBCT. Literature usually reports a range of doses to phantom volumes or organs for MV imaging (Gayou 2007, Li 2018). Tomotherapy, which utilizes a fanbeam MV-CT, has the multiple scan average dose metric with doses typically 1–3 cGy (Langen 2010), though it has not been adapted to MV-CBCT. In this study both kV- and MV-CBCT techniques were evaluated using CTDI to force a direct comparison. The dose distribution will be more central in the phantom for the megavoltage techniques, so the CTDI calculation may not be the optimal method to reflect imaging dose in a single value. However, the results of 23 mGy for kV and 33 mGy for MV give assurance that the MV dose is on the same order of magnitude as the kV dose, and the image quality gains are not coming solely at the expense of patient dose. The 8 MUs used for the MV-CBCTs in this study is also in line with the 2–15 MU values reported in the literature (Ding 2018). Additionally, if the MV imaging beam is modeled in the treatment planning system, it is straightforward to calculate and account for the imaging dose when treatment planning (Miften 2007, Alaei 2015).

The physics explaining the differences in the kV-CBCT and MV-CBCT findings is straightforward. MV photons interact primarily through Compton scattering, which depends on mass density instead of the atomic number Z. kV photons, by contrast, interact primarily by photoelectric effect and have a strong Z dependence. Thus MV-CBCT is more penetrative for high-Z objects but less sensitive to small variations in Z for soft tissue. This study demonstrates that MV-CBCT with a multilayer flat panel, whose architecture facilitates enhanced contrast and greater DQE, performs significantly better than the conventional single-layer flat panel. In addition, the MLI partially closes the gap on kV-CBCT performance and provides better images than kV-CBCT when metal implants are present.

Future applications of MV-CBCT using the MLI may include a role in adaptive planning. Prior research has demonstrated the accuracy of calibrating MV-CBCT for use in dose calculations (Petit 2008, Held 2015) using a standard EPID, and this task could be expected to benefit from an improved flat panel imager (Shi 2020). Results from the current

study suggest a strong benefit in adaptive planning particularly when there is metal near the treatment region. Additionally, the benefits of combining MV-CBCT with kV-CBCT (Lindsay 2019, Jacobson 2021) could be further explored. This study can also be expanded to other anatomical areas, as metal implants can be present in regions other than the pelvis, such as dental implants in the head and spinal fixation hardware.

Improved MV-CBCT using the MLI may also help expand radiation therapy access in under-resourced environments (Maitre 2022). Improved MV-CBCT could reduce the need for kV-CBCT imaging, reducing the initial investment burden as well as service costs both in terms of financial and uptime, without sacrificing quality care. MV-CBCT may also serve as a substitute for a CT simulator in departments lacking routine access to a dedicated CT scanner, with the added advantage of more direct HU calculation, compared to fan-beam kV imaging.

5. Conclusion

We demonstrated that megavoltage volumetric imaging has some advantages over kilovoltage imaging, particularly in situations where metal artifacts are present. MV-CBCT image sets were acquired with a multi-layer MV imager on a Varian TrueBeam clinical linear accelerator operating in Developer Mode. In comparison with kV-CBCT acquired with a standard pelvis imaging protocol, MV-CBCT using the novel multilayer imager demonstrated performance approaching that of kV-CBCT in the presence of normal anatomy and exceeding kV-CBCT in the presence of artifact-inducing metal implants. MV-CBCT taken by an MLI shows great promise as an alternative or in addition to kV-CBCT without compromising clinical care.

Acknowledgements

Research reported in this publication was supported by the National Cancer Institute of the National Institutes of Health under award number R01CA188446. The content is solely the responsibility of the authors and does not necessarily represent the official views of the National Institutes of Health.

References

Abbasian P, McCowan PM, Rickey DW, Van Uytven E, McCurdy BMC. Modeling the temporal-spatial nature of the readout of an electronic portal imaging device (EPID). Med Phys. 2020 Oct;47(10):5301–5311. doi: 10.1002/mp.14440. Epub 2020 Sep 2. [PubMed: 32762044]

Alaei P, Spezi E. Imaging dose from cone beam computed tomography in radiation therapy. Phys Med. 2015 Nov;31(7):647–58. doi: 10.1016/j.ejmp.2015.06.003. Epub 2015 Jul 4. [PubMed: 26148865]

Antonuk LE. Electronic portal imaging devices: a review and historical perspective of contemporary technologies and research. Phys Med Biol. 2002 Mar 21;47(6):R31–65. [PubMed: 11936185]

Barrett JF, Keat N. Artifacts in CT: recognition and avoidance. Radiographics. 2004 Nov-Dec;24(6):1679–91. doi: 10.1148/rg.246045065. [PubMed: 15537976]

Bujold A, Craig T, Jaffray D, Dawson LA. Image-guided radiotherapy: has it influenced patient outcomes? Semin Radiat Oncol. 2012 Jan;22(1):50–61. doi: 10.1016/j.semradonc.2011.09.001. [PubMed: 22177878]

Dawson LA, Jaffray DA. Advances in image-guided radiation therapy. J Clin Oncol. 2007 Mar 10;25(8):938–46. doi: 10.1200/JCO.2006.09.9515. [PubMed: 17350942]

Dice Lee R. (1945). “Measures of the Amount of Ecologic Association Between Species”. Ecology. 26 (3):297–302. doi:10.2307/1932409

Ding GX, Alaei P, Curran B, Flynn R, Gossman M, Mackie TR, Miften M, Morin R, Xu XG, Zhu TC. Image guidance doses delivered during radiotherapy: Quantification, management, and reduction: Report of the AAPM Therapy Physics Committee Task Group 180. Med Phys. 2018 May;45(5):e84–e99. doi: 10.1002/mp.12824. Epub 2018 Mar 24. [PubMed: 29468678]

Falcinelli L, Palumbo I, Radicchia V, Arcidiacono F, Lancellotta V, Montesi G, Matrone F, Zucchetti C, Marcantonini M, Bini V, Aristei C. Prostate cancer: contouring target and organs at risk by kilovoltage and megavoltage CT and MRI in patients with and without hip prostheses. Br J Radiol. 2015;88(1056):20150509. doi: 10.1259/bjr.20150509. Epub 2015 Oct 14. [PubMed: 26462970]

Feldkamp LA, Davis LC and Kress JW (1984) 'Practical cone-beam algorithm', Journal of the Optical Society of America A, 1(6), p. 612. doi: 10.1364/JOSAA.1.000612.

Gayou O, Parda DS, Johnson M, Miften M. Patient dose and image quality from mega-voltage cone beam computed tomography imaging. Med Phys. 2007 Feb;34(2):499–506. doi: 10.1118/1.2428407. [PubMed: 17388167]

Glide-Hurst CK, Lee P, Yock AD, Olsen JR, Cao M, Siddiqui F, Parker W, Doemer A, Rong Y, Kishan AU, Benedict SH, Li XA, Erickson BA, Sohn JW, Xiao Y, Wuthrick E. Adaptive Radiation Therapy (ART) Strategies and Technical Considerations: A State of the ART Review From NRG Oncology. Int J Radiat Oncol Biol Phys. 2021 Mar 15;109(4):1054–1075. doi: 10.1016/j.ijrobp.2020.10.021. Epub 2020 Oct 24. [PubMed: 33470210]

Groh BA, Siewerdsen JH, Drake DG, Wong JW, Jaffray DA. A performance comparison of flat-panel imager-based MV and kV cone-beam CT. Med Phys. 2002 Jun;29(6):967–75. doi: 10.1118/1.1477234. [PubMed: 12094992]

Harris TC, Seco J, Ferguson D, Lehmann M, Huber P, Shi M, Jacobson M, Valencia Lozano I, Myronakis M, Baturin P, Fueglistaller R, Morf D, Berbeco R. Clinical translation of a new flat-panel detector for beam's-eye-view imaging. Phys Med Biol. 2020 Dec 7;65(22):225004. doi: 10.1088/1361-6560/abb571. [PubMed: 33284786]

Harris TC, Seco J, Ferguson D, Jacobson M, Myronakis M, Lozano IV, Lehmann M, Huber P, Fueglistaller R, Morf D, Mamon HJ, Mancias JD, Martin NE, Berbeco RI. Improvements in beam's eye view fiducial tracking using a novel multilayer imager. Phys Med Biol. 2021 Jul 20;66(15). doi: 10.1088/1361-6560/ac1246.

Held M, Cremers F, Sneed PK, Braunstein S, Fogh SE, Nakamura J, Barani I, Perez-Andujar A, Pouliot J, Morin O. Assessment of image quality and dose calculation accuracy on kV CBCT, MV CBCT, and MV CT images for urgent palliative radiotherapy treatments. J Appl Clin Med Phys. 2016 Mar 8;17(2):279–290. doi: 10.1120/jacmp.v17i2.6040. [PubMed: 27074487]

Held M, Sneed PK, Fogh SE, Pouliot J, Morin O. Feasibility of MV CBCT-based treatment planning for urgent radiation therapy: dosimetric accuracy of MV CBCT-based dose calculations. J Appl Clin Med Phys. 2015 Nov 8;16(6):458–471. doi: 10.1120/jacmp.v16i6.5625. [PubMed: 26699575]

Hu YH, Rottmann J, Fueglistaller R, Myronakis M, Wang A, Huber P, Shedlock D, Morf D, Baturin P, Star-Lack J, Berbeco R. Leveraging multi-layer imager detector design to improve low-dose performance for megavoltage cone-beam computed tomography. Phys Med Biol. 2018 Jan 30;63(3):035022. doi: 10.1088/1361-6560/aaa160. [PubMed: 29235440]

Hu YH, Shedlock D, Wang A, Rottmann J, Baturin P, Myronakis M, Huber P, Fueglistaller R, Shi M, Morf D, Star-Lack J, Berbeco RI. Characterizing a novel scintillating glass for application to megavoltage cone-beam computed tomography. Med Phys. 2019 Mar;46(3):1323–1330. doi: 10.1002/mp.13355. Epub 2019 Feb 14. [PubMed: 30586163]

Hughes J, Holloway LC, Quinn A, Fielding A. An investigation into factors affecting electron density calibration for a megavoltage cone-beam CT system. J Appl Clin Med Phys. 2012 Sep 6;13(5):3271. doi: 10.1120/jacmp.v13i5.3271. [PubMed: 22955638]

Jacobson MW, Lehmann M, Huber P, Wang A, Myronakis M, Shi M, Ferguson D, Valencia-Lozano I, Hu YH, Baturin P, Harris T, Fueglistaller R, Williams C, Morf D, Berbeco R. Abbreviated on-treatment CBCT using roughness penalized mono-energization of kV-MV data and a multi-layer MV imager. Phys Med Biol. 2021 Jun 21;66(13). doi: 10.1088/1361-6560/abddd2.

Jaffray DA, Siewerdsen JH, Wong JW, Martinez AA. Flat-panel cone-beam computed tomography for image-guided radiation therapy. Int J Radiat Oncol Biol Phys. 2002 Aug 1;53(5):1337–49. doi: 10.1016/s0360-3016(02)02884-5. [PubMed: 12128137]

Jeon H, Park D, Youn H, Nam J, Lee J, Kim W, Ki Y, Kim YH, Lee JH, Kim D, Kim HK. Generation of hybrid sinograms for the recovery of kV-CT images with metal artifacts for helical tomotherapy. Med Phys. 2015 Aug;42(8):4654–67. doi: 10.1118/1.4926552. [PubMed: 26233193]

Joseph PM, Spital RD. A method for correcting bone induced artifacts in computed tomography scanners. J Comput Assist Tomogr. 1978 Jan;2(1):100–8. doi: 10.1097/00004728-197801000-00017. [PubMed: 670461]

Landry G, Dedes G, Zöllner C, Handrack J, Janssens G, Orban de Xivry J, Reiner M, Paganelli C, Riboldi M, Kamp F, Söhn M, Wilkens JJ, Baroni G, Belka C, Parodi K. Phantom based evaluation of CT to CBCT image registration for proton therapy dose recalculation. Phys Med Biol. 2015 Jan 21;60(2):595–613. doi: 10.1088/0031-9155/60/2/595. Epub 2014 Dec 30. [PubMed: 25548912]

Langen KM, Papanikolaou N, Balog J, Crilly R, Followill D, Goddu SM, Grant W 3rd, Olivera G, Ramsey CR, Shi C; AAPM Task Group 148. QA for helical tomotherapy: report of the AAPM Task Group 148. Med Phys. 2010 Sep;37(9):4817–53. doi: 10.1118/1.3462971. [PubMed: 20964201]

Li Y, Netherton T, Nitsch PL, Balter PA, Gao S, Klopp AH, Court LE. Normal tissue doses from MV image-guided radiation therapy (IGRT) using orthogonal MV and MV-CBCT. J Appl Clin Med Phys. 2018 May;19(3):52–57. doi: 10.1002/acm2.12276. Epub 2018 Mar 3. [PubMed: 29500856]

Lindsay C, Bazalova-Carter M, Wang A, Shedlock D, Wu M, Newson M, Xing L, Ansbacher W, Fahrig R, Star-Lack J. Investigation of combined kV/MV CBCT imaging with a high-DQE MV detector. Med Phys. 2019 Feb;46(2):563–575. doi: 10.1002/mp.13291. Epub 2018 Dec 6. [PubMed: 30428131]

Maitre P, Krishnatry R, Chopra S, Gondhowiardjo S, Likonda BM, Hussain QM, Zubizarreta EH, Agarwal JP. Modern Radiotherapy Technology: Obstacles and Opportunities to Access in Low- and Middle-Income Countries. JCO Glob Oncol. 2022 Jul;8:e2100376. doi: 10.1200/GO.21.00376. [PubMed: 35839434]

Miften M, Gayou O, Reitz B, Fuhrer R, Leicher B, Parda DS. IMRT planning and delivery incorporating daily dose from mega-voltage cone-beam computed tomography imaging. Med Phys. 2007 Oct;34(10):3760–7. doi: 10.1118/1.2779127. [PubMed: 17985621]

Morin O, Chen J, Aubin M, Gillis A, Aubry JF, Bose S, Chen H, Descovich M, Xia P, Pouliot J. Dose calculation using megavoltage cone-beam CT. Int J Radiat Oncol Biol Phys. 2007 Mar 15;67(4):1201–10. doi: 10.1016/j.ijrobp.2006.10.048. [PubMed: 17336221]

Mosleh-Shirazi MA, Evans PM, Swindell W, Webb S, Partridge M. A cone-beam megavoltage CT scanner for treatment verification in conformal radiotherapy. Radiother Oncol. 1998 Sep;48(3):319–28. doi: 10.1016/s0167-8140(98)00042-5. [PubMed: 9925252]

Myronakis M, Hu YH, Fueglistaller R, Wang A, Baturin P, Huber P, Morf D, Star-Lack J, Berbeco R. Multi-layer imager design for mega-voltage spectral imaging. Phys Med Biol. 2018 May 10;63(10):105002. doi: 10.1088/1361-6560/aabe21. [PubMed: 29652670]

Myronakis M, Huber P, Lehmann M, Fueglistaller R, Jacobson M, Hu YH, Baturin P, Wang A, Shi M, Harris T, Morf D, Berbeco R. Low-dose megavoltage cone-beam computed tomography using a novel multi-layer imager (MLI). Med Phys. 2020 Apr;47(4):1827–1835. doi: 10.1002/mp.14017. Epub 2020 Jan 28. [PubMed: 31930516]

Park S, Plishker W, Quon H, Wong J, Shekhar R, Lee J. Deformable registration of CT and cone-beam CT with local intensity matching. Phys Med Biol. 2017 Feb 7;62(3):927–947. doi: 10.1088/1361-6560/aa4f6d. Epub 2017 Jan 11. [PubMed: 28074785]

Petit SF, van Elmpt WJ, Nijsten SM, Lambin P, Dekker AL. Calibration of megavoltage cone-beam CT for radiotherapy dose calculations: correction of cupping artifacts and conversion of CT numbers to electron density. Med Phys. 2008 Mar;35(3):849–65. doi: 10.1118/1.2836945. [PubMed: 18404922]

Seppi EJ, Munro P, Johnsen SW, Shapiro EG, Tognina C, Jones D, Pavkovich JM, Webb C, Mollov I, Partain LD, Colbeth RE. Megavoltage cone-beam computed tomography using a high-efficiency image receptor. Int J Radiat Oncol Biol Phys. 2003 Mar 1;55(3):793–803. doi: 10.1016/s0360-3016(02)04155-x. [PubMed: 12573767]

Shi M, Myronakis M, Jacobson M, Ferguson D, Williams C, Lehmann M, Baturin P, Huber P, Fueglistaller R, Lozano IV, Harris T, Morf D, Berbeco RI. GPU-accelerated Monte Carlo

simulation of MV-CBCT. Phys Med Biol. 2020 Dec 2;65(23):235042. doi: 10.1088/1361-6560/abaeba. [PubMed: 33263311]

Shope TB, Gagne RM, Johnson GC. A method for describing the doses delivered by transmission x-ray computed tomography. Med Phys. 1981 Jul-Aug;8(4):488–95. doi: 10.1118/1.594995. [PubMed: 7322067]

Star-Lack J, Shedlock D, Swahn D, Humber D, Wang A, Hirsh H, Zentai G, Sawkey D, Kruger I, Sun M, Abel E, Virshup G, Shin M, Fahrig R. A piecewise-focused high DQE detector for MV imaging. Med Phys. 2015 Sep;42(9):5084–99. doi: 10.1118/1.4927786. [PubMed: 26328960]

Sun M, Star-Lack JM. Improved scatter correction using adaptive scatter kernel superposition. Phys Med Biol. 2010 Nov 21;55(22):6695–720. doi: 10.1088/0031-9155/55/22/007. Epub 2010 Oct 28. [PubMed: 21030750]

Thomas TH, Devakumar D, Purnima S, Ravindran BP. The adaptation of megavoltage cone beam CT for use in standard radiotherapy treatment planning. Phys Med Biol. 2009 Apr 7;54(7):2067–77. doi: 10.1088/0031-9155/54/7/014. Epub 2009 Mar 13. [PubMed: 19287087]

Valencia Lozano I, Shi M, Myronakis M, Baturin P, Fueglistaller R, Huber P, Lehmann M, Morf D, Ferguson D, Jacobson MW, Harris T, Berbeco RI, Williams CL. Frequency-dependent optimal weighting approach for megavoltage multilayer imagers. Phys Med Biol. 2021 Apr 16;66(8):10.1088/1361–6560/abe051. doi: 10.1088/1361-6560/abe051.

Wang Z, Bovik AC, Sheikh HR, Simoncelli EP. Image quality assessment: from error visibility to structural similarity. IEEE Trans Image Process. 2004 Apr;13(4):600–12. doi: 10.1109/tip.2003.819861. [PubMed: 15376593]

Wellenberg RH, Boomsma MF, van Osch JA, Vlassenbroek A, Milles J, Edens MA, Streekstra GJ, Slump CH, Maas M. Quantifying metal artefact reduction using virtual monochromatic dual-layer detector spectral CT imaging in unilateral and bilateral total hip prostheses. Eur J Radiol. 2017 Mar;88:61–70. doi: 10.1016/j.ejrad.2017.01.002. Epub 2017 Jan 4. [PubMed: 28189210]

Wu M, Keil A, Constantin D, Star-Lack J, Zhu L, Fahrig R. Metal artifact correction for x-ray computed tomography using kV and selective MV imaging. Med Phys. 2014 Dec;41(12):121910. doi: 10.1118/1.4901551. [PubMed: 25471970]

Zhao W, Ristic G, Rowlands JA. X-ray imaging performance of structured cesium iodide scintillators. Med Phys. 2004 Sep;31(9):2594–605. doi: 10.1118/1.1782676. [PubMed: 15487742]

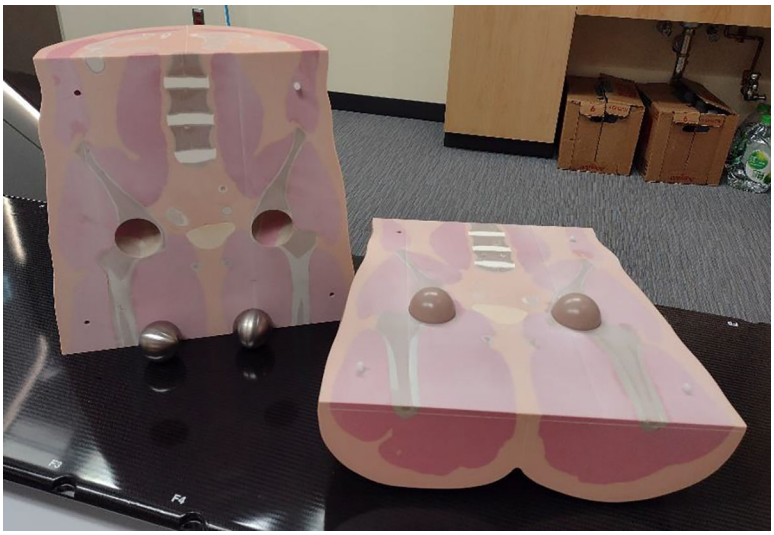

Figure 1:
The custom anthropomorphic phantom with replaceable femoral head spheres – trabecular bone, titanium, and aluminum. The anterior half can be lifted off to allow easy swapping of the spheres without disturbing the phantom's positioning.

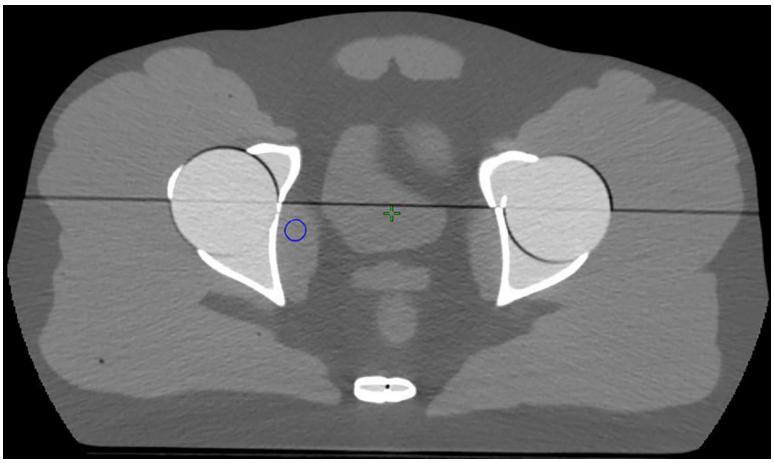

Figure 2a:
The ROI used to assess the effect on HU homogeneity is shown in blue. This ROI is expected to be most affected when metal inserts are present.

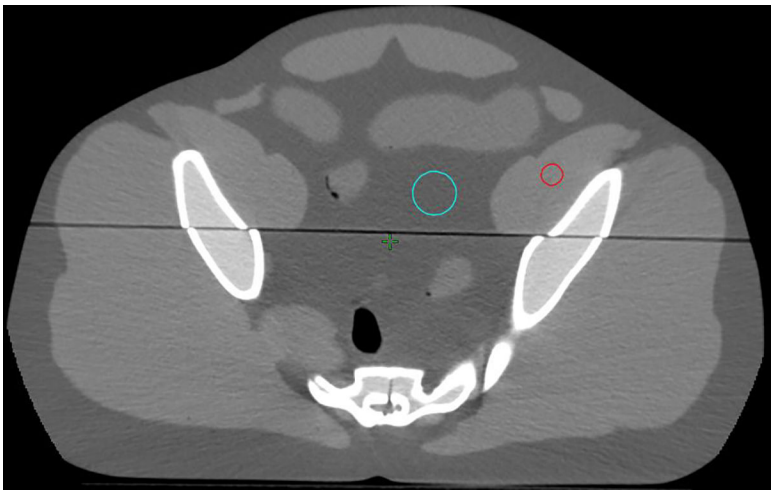

Figure 2b:
The ROIs used to assess the effect on HU homogeneity are shown in cyan and red. These contours are out of plane from the femoral heads and are expected to be less affected when metal inserts are used.

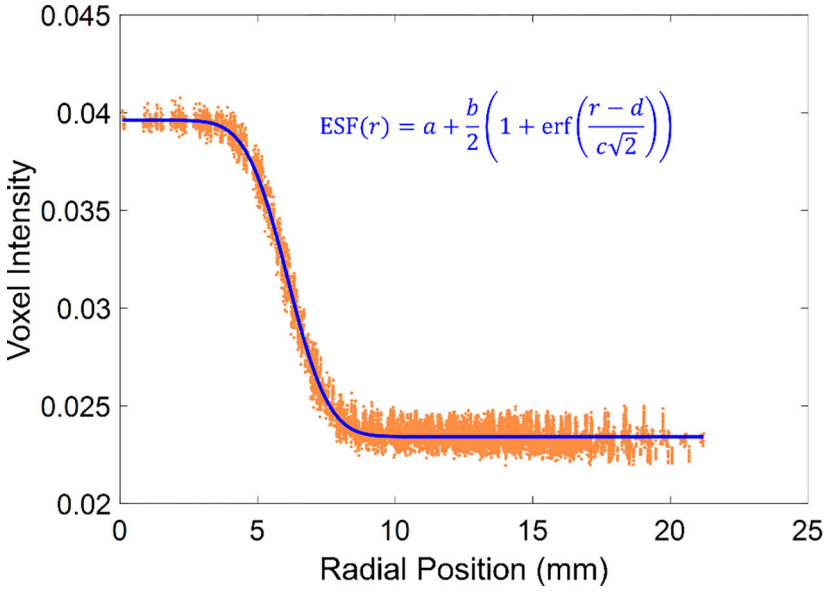

Figure 3:

Edge spread function analysis at the curved edge of the CatPhan 604's Teflon insert. Differentiating the ESF gives an estimate of the point spread function.

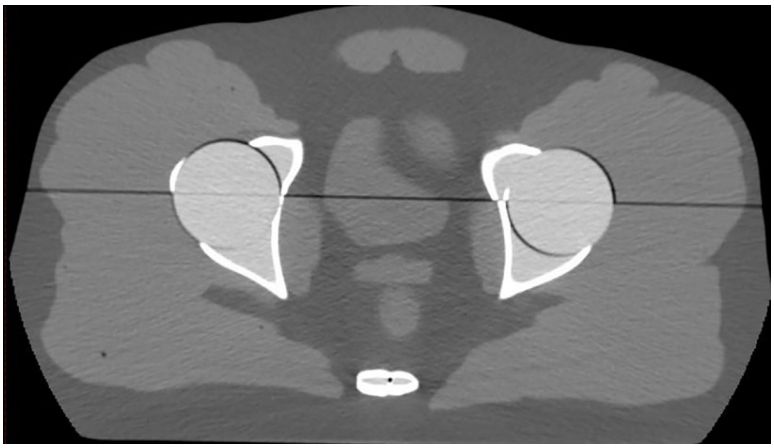

Figure 4:
A helical CT of the phantom with trabecular bone inserts. This scan is considered the ground truth for evaluating the CBCTs.

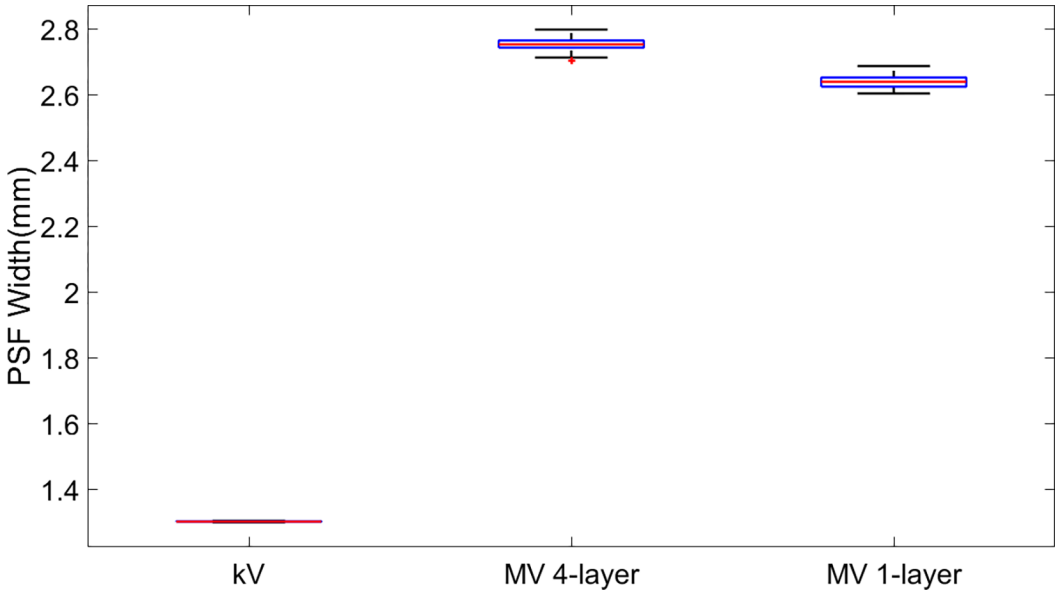

Figure 5:
A box and whisker plot of the point spread function. This was determined by differentiating the edge spread function across the interface of the Teflon insert in a CatPhan 604.

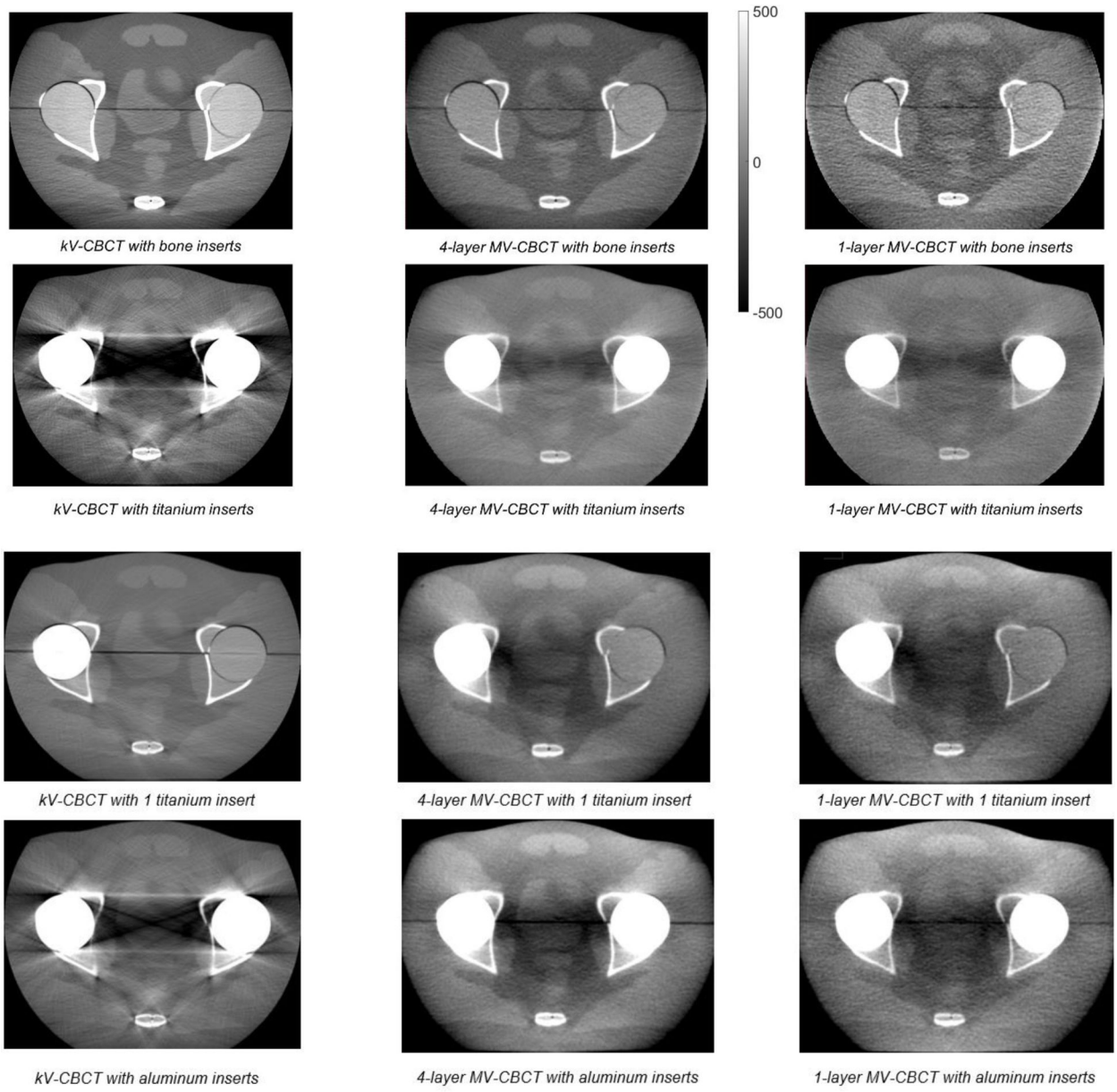

Figure 6:

All 12 CBCT reconstructions. The first room displays the response with normal anatomy, and the second row with the most adverse anatomy, bilateral titanium implants. Rows 3 and 4 show intermediate levels of metal artifact with a unilateral titanium implant and bilateral aluminum implants, respectively.

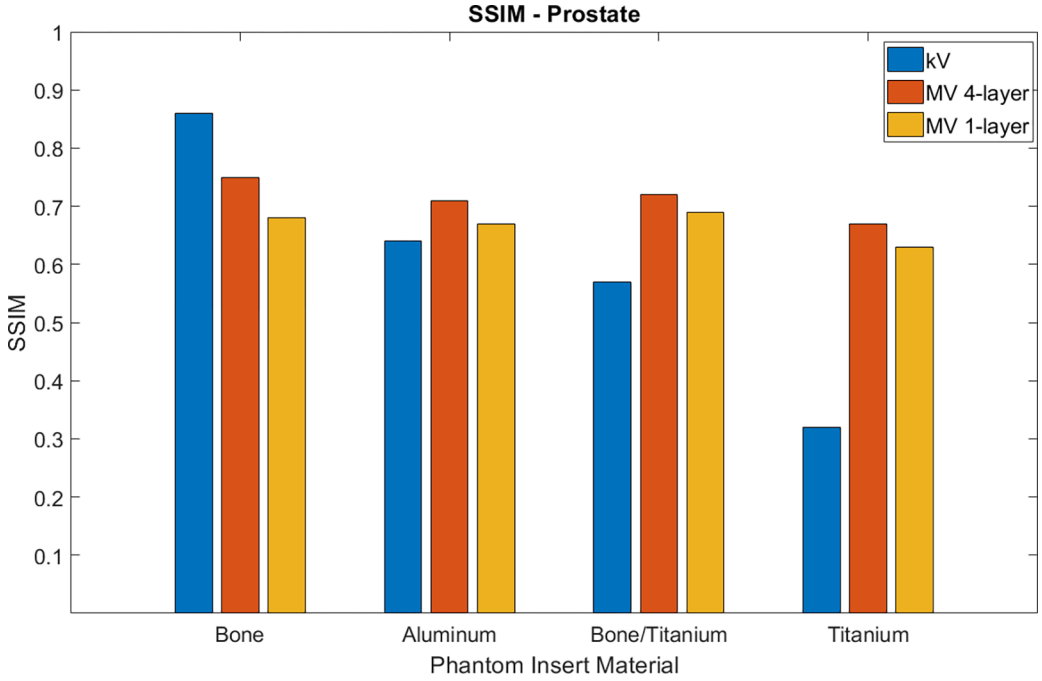

Figure 7a:

The calculated SSIM of the CT prostate contour compared to the same region on the CBCTs after rigid registration. kV has the highest SSIM in the absence of metal, with 4-layer MV approaching it's value. MV outperforms kV in the presence of metal, particularly with bilateral titanium implants.

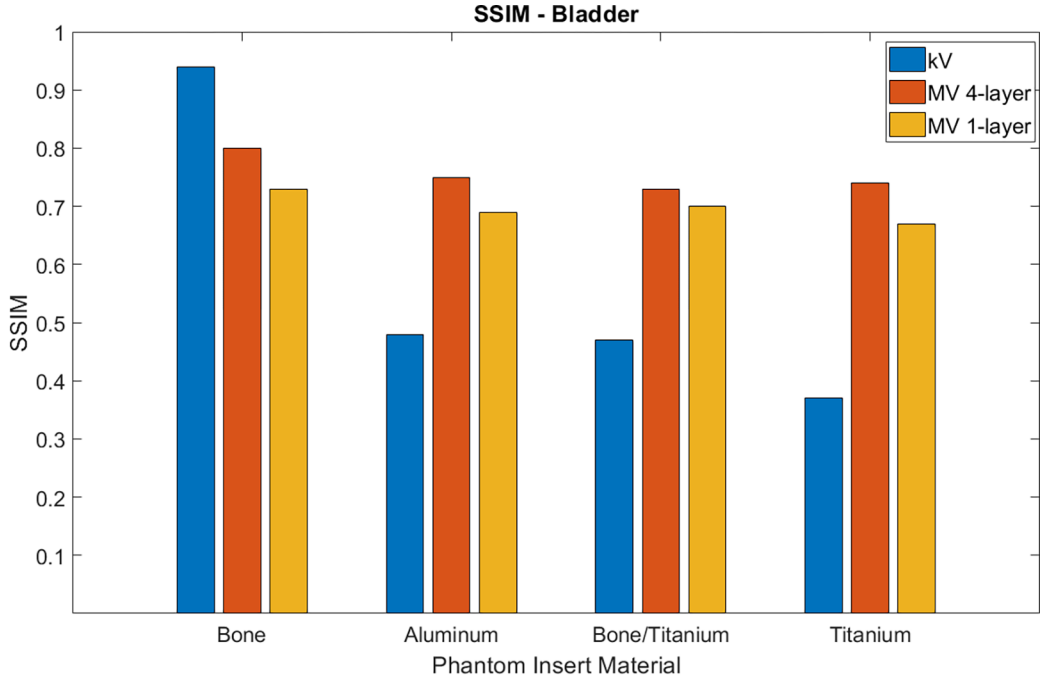

Figure 7b:

The calculated SSIM of the CT bladder contour compared to the same region on the CBCTs after rigid registration. Results follow a similar trend to the prostate results with MV showing higher performance in the presence of metal.

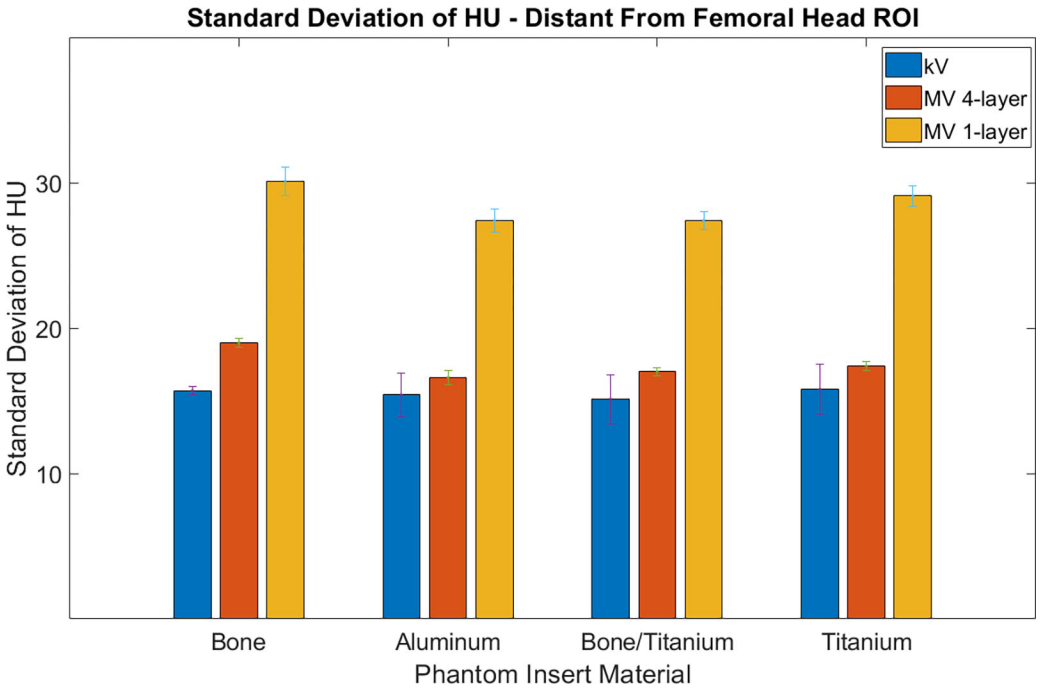

Figure 8a:

The standard deviation of the HU for ROIs distant and out of plane from the femoral heads. The 1-layer results are nearly double the 4-layer results, largely reflecting a ½ reduction in noise when collecting nearly 4x the number of photons.

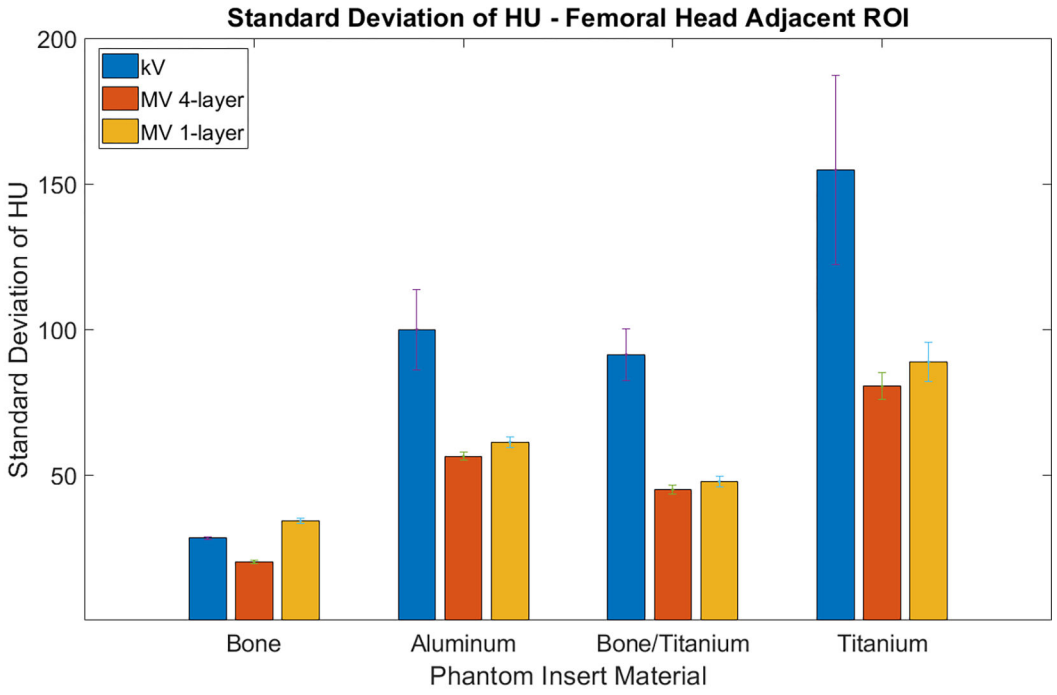

Figure 8b:

The standard deviation for the HU for ROIs in plane with the femoral heads and 0.5 to 1.5 cm away from the high density material. kV results have greater deviation even when the material is only trabecular bone.

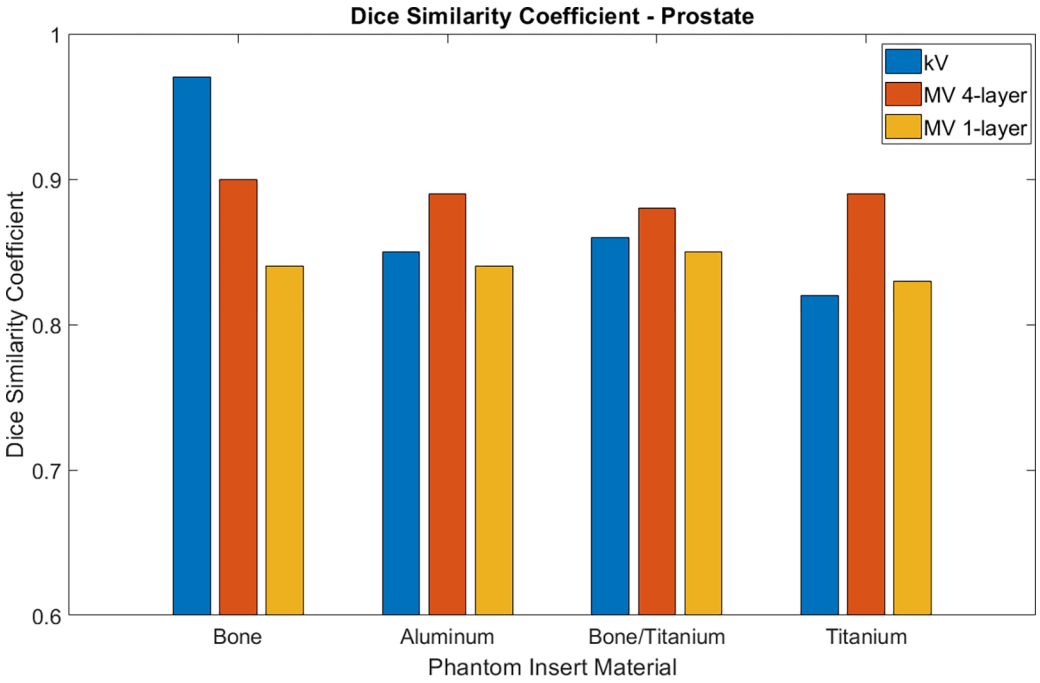

Figure 9a:

The calculated Dice Similarity Coefficient for prostate contours segmented on the CT compared to prostate contours segmented on the various CBCTs. MV-CBCT displays a modest increase in Dice compared to kV-CBCT in the presence of metal.

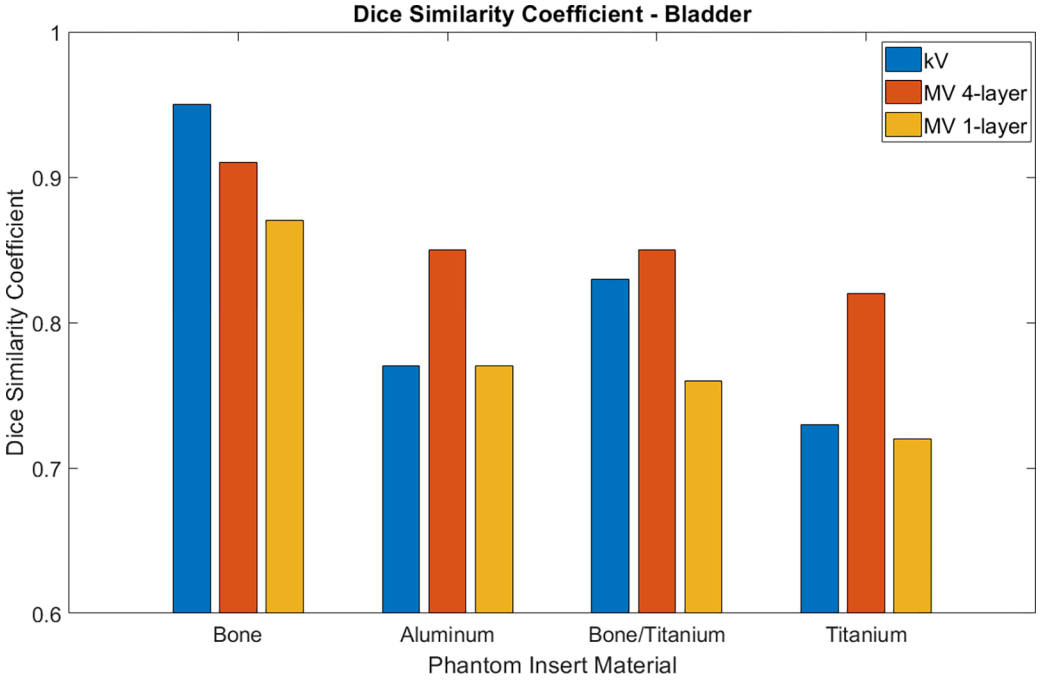

Figure 9b:

The calculated Dice Similarity Coefficient for bladder contours segmented on the CT compared to bladder contours segmented on the various CBCTs. MV-CBCT shows a small increase in Dice compared to kV-CBCT when metal is present.